



This is a repository copy of *Optimization of the failure criterion in micro-Finite Element models of the mouse tibia for the non-invasive prediction of its failure load in preclinical applications*.

White Rose Research Online URL for this paper:
<https://eprints.whiterose.ac.uk/168199/>

Version: Published Version

Article:

Oliviero, S., Owen, R., Reilly, G.C. et al. (2 more authors) (2021) Optimization of the failure criterion in micro-Finite Element models of the mouse tibia for the non-invasive prediction of its failure load in preclinical applications. *Journal of the Mechanical Behavior of Biomedical Materials*, 113. 104190. ISSN 1751-6161

<https://doi.org/10.1016/j.jmbbm.2020.104190>

Reuse

This article is distributed under the terms of the Creative Commons Attribution (CC BY) licence. This licence allows you to distribute, remix, tweak, and build upon the work, even commercially, as long as you credit the authors for the original work. More information and the full terms of the licence here:
<https://creativecommons.org/licenses/>

Takedown

If you consider content in White Rose Research Online to be in breach of UK law, please notify us by emailing eprints@whiterose.ac.uk including the URL of the record and the reason for the withdrawal request.



eprints@whiterose.ac.uk
<https://eprints.whiterose.ac.uk/>



Contents lists available at ScienceDirect

Journal of the Mechanical Behavior of Biomedical Materials

journal homepage: <http://www.elsevier.com/locate/jmbbm>

Optimization of the failure criterion in micro-Finite Element models of the mouse tibia for the non-invasive prediction of its failure load in preclinical applications

S. Oliviero^{a,b}, R. Owen^{b,c,d}, G.C. Reilly^{b,c}, I. Bellantuono^{a,b,e}, E. Dall'Ara^{a,b,*}

^a Department of Oncology and Metabolism, Mellanby Centre for Bone Research, University of Sheffield, UK

^b INSIGNEO Institute for in Silico Medicine, University of Sheffield, UK

^c Department of Materials Science and Engineering, University of Sheffield, UK

^d Regenerative Medicine and Cellular Therapies, School of Pharmacy, University of Nottingham Biodiscovery Institute, University Park, UK

^e Healthy Lifespan Institute, Department of Oncology and Metabolism, The Medical School, University of Sheffield, UK

ARTICLE INFO

Keywords:

Mouse tibia
microCT
Validation
Stiffness
Failure load
Finite element

ABSTRACT

New treatments against osteoporosis require testing in animal models and the mouse tibia is among the most common studied anatomical sites. *In vivo* micro-Computed Tomography (microCT) based micro-Finite Element (microFE) models can be used for predicting the bone strength non-invasively, after proper validation against experiments. The aim of this study was to evaluate the ability of different microCT-based bone parameters and microFE models to predict tibial structural mechanical properties in compression. Twenty tibiae were scanned at 10.4 μm voxel size and subsequently tested in uniaxial compression at 0.03 mm/s until failure. Stiffness and failure load were measured from the load-displacement curves. Standard morphometric parameters were measured from the microCT images. The spatial distribution of bone mineral content (BMC) was evaluated by dividing the tibia into 40 regions. MicroFE models were generated by converting each microCT image into a voxel-based mesh with homogeneous isotropic material properties. Failure load was estimated by using different failure criteria, and the optimized parameters were selected by minimising the errors with respect to experimental measurements. Experimental and predicted stiffness were moderately correlated ($R^2 = 0.65$, error = $14\% \pm 8\%$). Normalized failure load was best predicted by microFE models ($R^2 = 0.81$, error = $9\% \pm 6\%$). Failure load was not correlated to the morphometric parameters and weakly correlated with some geometrical parameters ($R^2 < 0.37$). In conclusion, microFE models can improve the current estimation of the mouse tibia structural properties and in this study an optimal failure criterion has been defined. Since it is a non-invasive method, this approach can be applied longitudinally for evaluating temporal changes in the bone strength.

1. Introduction

Osteoporosis and osteoarthritis are the most common chronic diseases of the musculoskeletal system. Animal models are fundamental for the development and testing of new bone physical or pharmacological interventions before clinical translation, and the mouse is among the most common models for the ability of controlling the environment, the relatively low costs, and the possibility of performing high-resolution assessment of bone and other musculoskeletal tissues (Bouxsein et al., 2010). In terms of clinical translation, bone strength is a relevant endpoint and many studies have focused on the development of tools for the accurate prediction of strength in the human femur and vertebra

under relevant loading conditions (Keaveny et al., 2014; Qasim et al., 2016; Zysset et al., 2015). Nevertheless, in preclinical studies the strength of the mouse tibia is commonly measured using three-point bending tests (Jepsen et al., 2015), which presents a number of limitations. First, these tests are invasive and they can only be performed *ex vivo* in cross-sectional experiments, which are associated to the usage of a large number of animals. Second, three-point bending is not representative of the physiological loading conditions, which would be better replicated by compressive tests (Holguin et al., 2013). Third, this testing approach is affected by experimental artifacts, mainly due to the fact that the aspect ratio of the tibia is low and its cross-section is not constant along the longitudinal direction (Wallace et al., 2014). In order to

* Corresponding author. Department of Oncology and Metabolism, Mellanby Centre for Bone Research, University of Sheffield, UK.

E-mail address: e.dallara@sheffield.ac.uk (E. Dall'Ara).

<https://doi.org/10.1016/j.jmbbm.2020.104190>

Received 23 April 2020; Received in revised form 23 September 2020; Accepted 27 October 2020

Available online 2 November 2020

1751-6161/© 2020 The Authors. Published by Elsevier Ltd. This is an open access article under the CC BY license (<http://creativecommons.org/licenses/by/4.0/>).

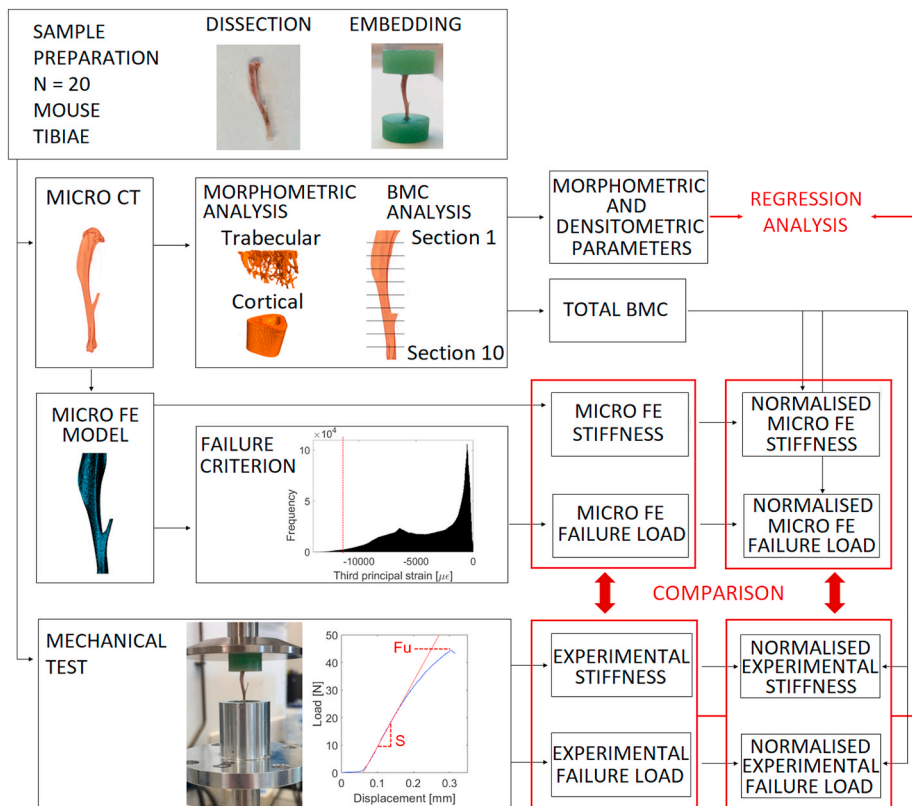


Fig. 1. Overview of the methods. Each tibia was dissected and the extremities were embedded in resin. A microCT scan was acquired for each tibia. Morphometric and densitometric parameters were measured from microCT images. The microCT scans were also used to generate specimen-specific microFE models. Subsequently, each tibia was tested in compression. From the experimental curves, stiffness (S) and failure load (F_u) were measured. Mechanical properties were estimated from the models and compared to the experimental measurements. Total bone mineral content (BMC) was used to normalize the mechanical properties. Regression analyses were used to determine the ability of morphometric or densitometric parameters in predicting the experimental mechanical properties.

overcome these limitations, micro-Finite Element (microFE) models can be used for predicting bone strength under compression non-invasively, if properly validated against experiments. In particular, this approach based on *in vivo* micro-Computed Tomography (microCT) can be utilised in a longitudinal experimental design (Dall'ara et al., 2016), to dramatically reduce the usage of mice in bone research, in line with the 3Rs (replacement, refinement and reduction of the usage of animals in research) (Viceconti and Dall'ara, 2019).

MicroCT-based microFE models of the mouse tibia have been applied to study the effect of different bone interventions, including ovariectomy (Roberts et al., 2019), mechanical loading (Patel et al., 2014; Razi et al., 2015) and parathyroid hormone injections (Lu et al., 2017). Nevertheless, their validation against experimental data is limited. Some studies have validated the local strains predicted by microFE models against strain gauge measurements (Patel et al., 2014; Razi et al., 2015; Yang et al., 2017), which are limited to a few spatial locations over the tibia. Additionally, the application of the sensor itself may cause a local stiffening of the specimen, as shown for the mouse forearm (Begonia et al., 2017). Digital Image Correlation measurements have also been used to validate microFE strain distributions on the surface of the tibia (Pereira et al., 2015). Lastly, the local displacements of the tibia tested under compression in the elastic regime have been measured with Digital Volume Correlation and used to validate the microFE models outputs (Oliviero et al., 2018). However, the above studies mainly focused on validating the models at the local level and in the elastic range, while a comparison of the structural mechanical properties (stiffness and failure load) predictions versus experimental measurements is missing for the mouse tibia.

The predictions of structural properties from FE models have been extensively validated for different bone types (Zysset et al., 2013), such as trabecular bone specimens (Schwiedrzik et al., 2016; Wolfram et al., 2010), human vertebral bodies (Crawford et al., 2003; Dall'ara et al., 2012; Gustafson et al., 2017), human femur (Dall'ara et al., 2013; Pottecher et al., 2016; Schileo et al., 2008) and human distal radius

(Macneil and Boyd, 2008; Pistoia et al., 2002; Varga et al., 2011), while for mouse bones only a few validation studies have been reported. Nyman et al. (2015) evaluated the accuracy of microFE models for the prediction of the mouse vertebra strength in compression, as well as the influence of material properties definitions. They found good agreement between experiments and FE predictions ($R^2 = 0.62-0.89$), even though accuracy was dependant on the assigned material properties (Nyman et al., 2015). Varga et al. (2020) reported recently that the microFE approach could accurately predict mouse femur failure load in four-point bending tests, by comparison with experimental tests ($R^2 = 0.93$) (Varga et al., 2020). In these studies, the failure criterion used for mouse bones was based on outputs from linear models by assuming that bone fails when a certain number of elements are deformed beyond yield strain, adapting a rule originally defined by Pistoia et al. (2002) for the human distal radius. Nevertheless, the best failure criterion to predict the mouse tibia failure load under compression with microCT-based microFE is still unknown.

The aim of this study was to evaluate the ability of morphological and densitometric properties estimated from *in vivo* microCT and structural properties estimated with microFE models to predict experimentally measured structural mechanical properties of the mouse tibia when loaded in compression.

2. Materials and methods

An overview of the methods used in this study is presented in Fig. 1. Briefly, twenty mouse tibiae were microCT scanned and subsequently tested under compression. The microCT images were used to generate specimen-specific microFE models for the prediction of structural mechanical properties of the tibia. From the experimental curves, stiffness and failure load of each tibia were obtained. Finally, the best predictor of experimentally measured mechanical properties from morphological, densitometric and estimated mechanical properties with the microFE models was identified with regression analyses.

Table 1

Properties of the tested mouse tibiae. WT = wild type, OVX = ovariectomized, PTH = treated with parathyroid hormone injections. Parameters reported: BMC = bone mineral content, TMD = tissue mineral density, BV/TV = bone volume fraction.

N	Strain	Group	Age [weeks]	Side	BMC [mg]	TMD [mgHA/cc]	BV/TV [-]	Experimental Stiffness [N/mm]	Experimental Failure Load [N]
1	C57BL/6J	WT	16	Right	7.12	871	0.62	178	42.0
2	C57BL/6J	WT	16	Right	6.91	846	0.58	233	47.8
3	C57BL/6J	WT	24	Left	8.58	918	0.60	237	44.4
4	C57BL/6J	WT	24	Left	8.07	1087	0.59	195	39.2
5	C57BL/6J	OVX	16	Right	6.74	873	0.58	307	47.0
6	C57BL/6J	OVX	16	Left	6.28	866	0.57	287	42.8
7	C57BL/6J	OVX	24	Left	9.68	890	0.56	188	42.8
8	C57BL/6J	OVX	24	Left	7.63	893	0.55	236	45.1
9	C57BL/6J	PTH	24	Left	10.46	918	0.64	234	46.4
10	C57BL/6J	PTH	24	Left	10.24	923	0.62	366	56.4
11	C57BL/6J	PTH	24	Left	7.95	906	0.61	265	49.1
12	C57BL/6J	PTH	24	Left	7.95	849	0.61	333	55.5
13	BALB/c	WT	16	Right	11.36	1047	0.66	205	38.0
14	BALB/c	WT	16	Right	12.10	1094	0.65	147	40.5
15	BALB/c	WT	24	Right	10.79	1046	0.70	167	41.7
16	BALB/c	WT	24	Right	6.88	925	0.69	319	51.5
17	BALB/c	OVX	16	Right	8.15	897	0.65	235	48.6
18	BALB/c	OVX	16	Left	6.83	949	0.70	226	45.6
19	BALB/c	OVX	24	Right	10.77	1023	0.73	344	63.9
20	BALB/c	OVX	24	Right	10.04	1003	0.68	282	49.7

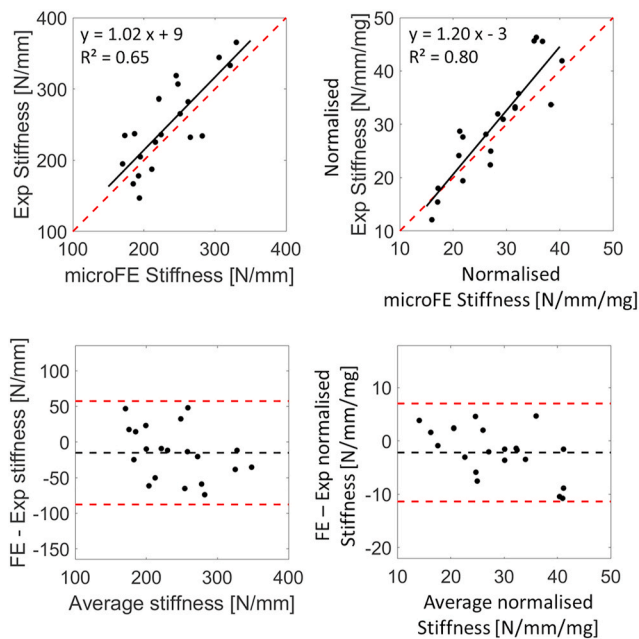


Fig. 2. Regression analysis and Bland-Altman plots between the microFE predictions and experimental measurements of stiffness. Normalized stiffness was obtained by dividing by the total bone mineral content (BMC, [mg]).

2.1. Sample preparation

Twenty mouse tibiae were dissected from female mice of different strains (C57BL/6J and BALB/c), ages (16 and 24 weeks) and intervention groups, collected from previous studies (Roberts et al., 2019). Details about the specimens are reported in Table 1. Samples from different groups of mice were selected in order to obtain a wide range of mechanical properties and to test the model predictions in different conditions. Groups included wild type mice (WT), ovariectomized mice (OVX, surgery performed at week 14 of age) and mice treated with parathyroid hormone (PTH, daily injections, 5 days/weeks from week 18 to 22 of age). Both left and right tibiae were included in the study.

After carefully removing the soft tissues and the fibula (cut above the tibio-fibular junction) with a scalpel, the specimens were dehydrated in

air at room temperature for 1 h. The length was measured with a caliper and the extremities were embedded in resin (Technovit 4071, Kulzer, Germany) up to 10% of the total length (Fig. 1), which facilitated the positioning in the loading machine and correspondence between loading conditions in the experiments and in the models. The alignment of each tibia was controlled with a custom-made jig that was also used for the mechanical testing. The tibiae were kept frozen at -20°C until testing.

2.2. Scanning procedures and reconstructions

Each tibia was defrosted and rehydrated at room temperature in saline solution for 3 h. The bone was wrapped in cling film in order to avoid dehydration during the microCT scan. The scanning procedure applied in this study has been previously defined for *in vivo* applications (VivaCT 80, Scanco Medical, Bruettisellen, Switzerland; 55 kVp, 145 μA , 10.4 μm voxel size, 100 ms integration time, 32 mm field of view, 750 projections/ 180° , no frame averaging, 0.5 mm Al filter) as a compromise between nominal radiation dose and accuracy in the measurement of bone properties (Oliviero et al., 2017). This protocol is associated with a nominal radiation dose of 256 mGy, which has minimal effects on bone properties (Oliviero et al., 2019). All images were reconstructed using software provided by the manufacturer (Scanco Medical AG) and applying a beam hardening correction based on a phantom of 1200 mg HA/cc density, which has been shown to improve the local tissue mineralization measurement (Kazakia et al., 2008). MicroCT images were used to generate specimen-specific microFE models, as well as to measure morphometric and densitometric parameters, in order to analyze their ability to predict the mechanical properties. Interested readers are welcome to contact the corresponding author who will share the data used in this study (<https://doi.org/10.15131/shef.data.13176131>).

2.3. Standard morphometric analysis

The procedure applied for morphometric analysis has been published previously (Oliviero et al., 2017, 2019) and is briefly summarized here. Standard morphometric analyses of trabecular and cortical regions of interest were performed in CTAn (Bruker, Belgium). For trabecular analysis, a reference cross-section was selected, identified as the one where the medial and lateral sides of the growth plate merged. The trabecular VOI started at an offset of 0.2 mm from the reference slice and extended 1 mm distally. Trabecular bone was contoured manually by

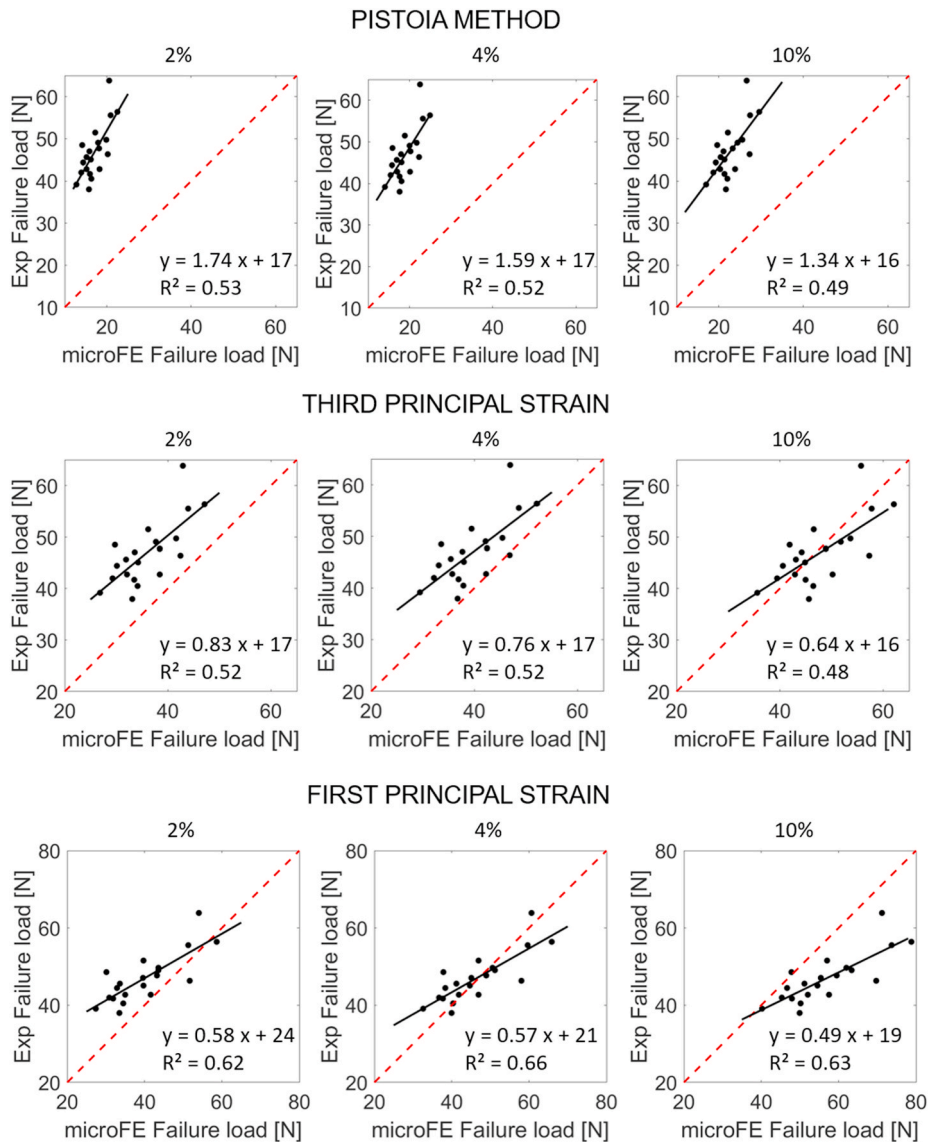


Fig. 3. Regression analysis between the experimental measurements and microFE predictions of failure load based on different failure criteria (Pistoia method, third principal strain with critical strain level of $-14420 \mu\epsilon$, first principal strain with critical strain level of $6400 \mu\epsilon$). For each criterion the results for three failure volume levels are reported (2%, 4% and 10%).

selecting 2D regions of interest every 5 slices. A single level threshold was used for segmentation, calculated for each tibia as the average of the grey levels corresponding to the bone and background peaks in the histogram. A despeckling filter was applied to remove 3D white (bone) regions less than 10 voxels in volume, which were attributed to non-filtered noise. Trabecular bone volume fraction (Tb.BV/TV), thickness (Tb.Th), separation (Tb.Sp) and number (Tb.N) were computed (Bouxsein et al., 2010).

For cortical analysis, a 1 mm thick region was centered at the tibial midshaft. After segmentation, pores within the cortex were removed by applying a closing function (2D round kernel, 10 pixels radius). Total cross-sectional area (Tt.Ar), cortical bone area (Ct.Ar), cortical area fraction (Ct.Ar/Tt.Ar) and cortical thickness (Ct.Th) were computed (Bouxsein et al., 2010). Cortical bone analyses were not performed in the proximal region due to the lack of reproducibility in identifying the cortical contour in that porous region.

2.4. Spatial distribution of BMC

The method used for analyzing the spatial distribution of BMC

(implemented using Matlab and using the raw 16 bit images) has been developed in previous studies by our group (Lu et al., 2016; Oliviero et al., 2017) and is summarized here. The attenuation coefficients acquired in the microCT images were converted into tissue mineral density (TMD) using the calibration law provided by the manufacturer of the scanner. Weekly quality checks were performed on a densitometric phantom with five insertions (800, 400, 200, 100 and 0 mg HA/cc) in order to monitor the stability of the calibration parameters. BMC in each voxel was calculated as its TMD multiplied by the volume of the voxel. A volume of interest (VOI) was selected by excluding the portions embedded in the resin (Fig. 1). Total BMC, TMD and BV/TV were computed in the VOI. The VOI was divided into ten longitudinal sections ("1" refers to the proximal tibia, "10" refers to the distal tibia). For each longitudinal section, the following parameters were measured: bone mineral content (BMC, [mg]), tissue mineral density (TMD, [mgHA/cc]), total bone volume fraction (BV/TV, [%], including both trabecular and cortical bone), total cross-sectional area (TA, [mm²]), bone area (BA, [mm²]), second moment of area in the antero-posterior direction (I_{xx} , [mm⁴]) and in the medio-lateral direction (I_{yy} , [mm⁴]), polar moment of inertia (I_{zz} , [mm⁴]). Each longitudinal section was also

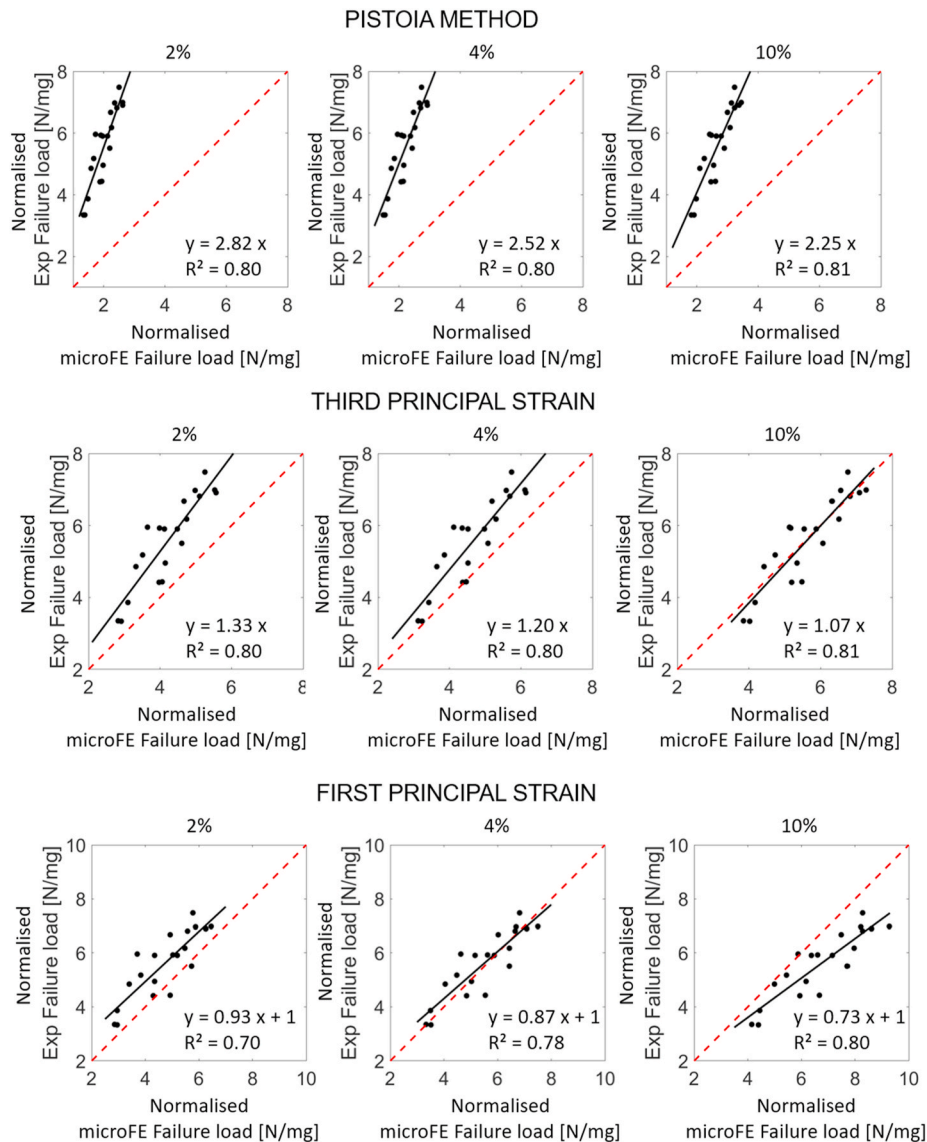


Fig. 4. Regression analysis between the experimental measurements and microFE predictions of failure load based on different failure criteria (Pistoia method, third principal strain with critical strain level of $-14420 \mu\epsilon$, first principal strain with critical strain level of $6400 \mu\epsilon$). For each criterion the results for three failure volume levels are reported (2%, 4% and 10%). Normalized failure load was obtained by dividing by the total bone mineral content (BMC, [mg]).

divided into four quadrants (anterior, posterior, medial and lateral), defined for each cross-section by two perpendicular lines containing its centroid (40 partitions in total), and BMC was calculated for each partition.

2.5. Mechanical tests in uniaxial compression

Each tibia was tested using a Bose Electroforce 3200 mechanical testing machine with a 450 N load cell. Bones were carefully positioned to align the embedding blocks to the axis of the loading machine (Fig. 1). Ten preconditioning cycles were applied at 0.042 Hz between 1 N and 4 N to achieve a steady viscoelastic state and to ensure stable boundary conditions during the test (Zhao et al., 2018). Afterwards, each bone was loaded in compression until failure at 0.03 mm/s (Holguin et al., 2013). Stiffness [N/mm] was measured from the load-displacement curve as the slope of the linear portion of the curve (Fig. 1). Failure load [N] was defined as the maximum load from the load-displacement curve (Fig. 1). Normalized failure load and stiffness were calculated by dividing the failure load and the stiffness by the total BMC in order to account for the size and overall mineralization of the specimens.

2.6. Micro-Finite Element models

In order to replicate the experimental alignment in the microFE models, each image was rigidly rotated so that the longitudinal axis corresponded to the loading direction of the testing machine. The lower surface of the embedding material was identified from the microCT image, fitted to a plane (affine fit function, Matlab) and aligned to the horizontal direction with a rigid rotation (Amira 6.0.0, FEI Visualization Sciences Group, France). After alignment, images were resampled using Lanczos interpolator (Birkhold et al., 2014). A Gaussian filter (kernel $3 \times 3 \times 3$, standard deviation 0.65) was applied to reduce the high frequency noise (Bouxsein et al., 2010).

The image was segmented by using a single level threshold, calculated as the average of the grey levels corresponding to the bone and background peaks in the image histogram (Christiansen, 2016). A connectivity filter was applied in order to remove unconnected voxels (connectivity rule equal to 6 keeping plane connectivity, bwlabeln function in Matlab). A Cartesian mesh was obtained by converting each bone voxel into an 8-noded hexahedral element (Chen et al., 2017; Costa et al., 2017; Patel et al., 2014) with isotropic linear elastic material

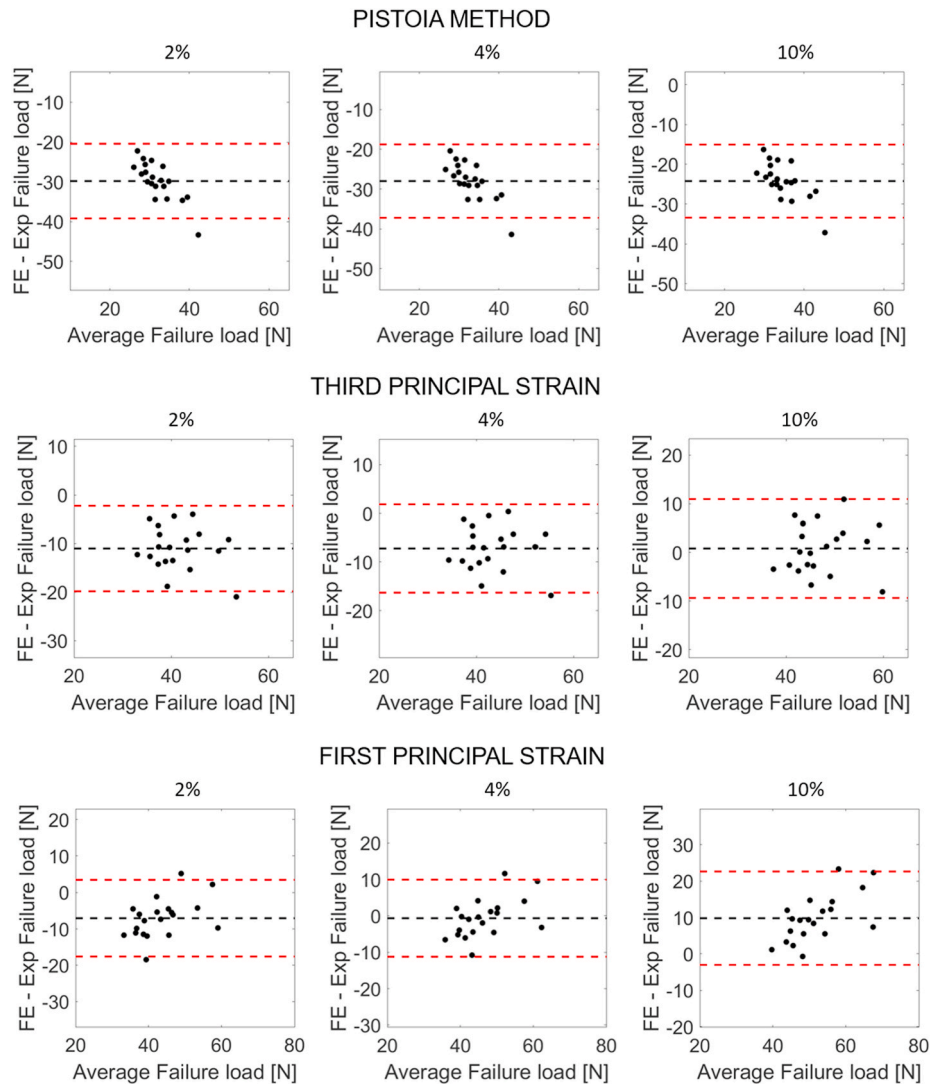


Fig. 5. Bland-Altman plots for the experimental measurements and microFE predictions of failure load based on different failure criteria (Pistoia method, third principal strain with critical strain level of $-14420 \mu\epsilon$, first principal strain with critical strain level of $6400 \mu\epsilon$). For each criterion the results for three failure volume levels are reported (2%, 4% and 10%).

properties (Young's Modulus = 14.8 GPa, Poisson's ratio = 0.3 (Oliviero et al., 2018)). The value of the Young's modulus chosen in this study for the homogenous microFE models is also in line with the mean elastic modulus measured from nanoindentation tests in the tibia of C57BL/6J and BALB/c female mice in a similar age range (Pepe et al., 2020). Uniaxial compression was simulated by fully constraining the distal end of the tibia and applying a displacement of 0.1 mm on each node of the proximal surface along the longitudinal direction. The apparent stiffness was calculated as the sum of reaction forces at the distal surface, divided by the applied displacement. For the estimation of failure load from linear microFE models, different failure criteria were defined based on the criterion introduced by (Pistoia et al., 2002) for the human distal radius, which assumed that the bone fails when a portion of the nodes reaches a critical strain level. For the distal radius, the parametric analysis determined the optimal parameters as failure volume equal to 2% of the nodes and critical effective strain level of $7000 \mu\epsilon$ (Pistoia et al., 2002). Similarly, in this study a parametric analysis was performed to determine the optimal volume of failed elements and the critical strain value for the mouse tibia, which provided the strongest correlation with the experimental results and the lowest errors. The following failure criteria were tested, based on strain analyses across the whole tibia:

- The tibia fails when a portion of the nodes (2%, 4%, 6%, 8% or 10%) reaches an effective strain level of $7000 \mu\epsilon$ (Pistoia et al., 2002).
- The tibia fails when a portion of the nodes (2%, 4%, 6%, 8% or 10%) reaches a critical compressive (third principal) strain of $-10300 \mu\epsilon$, which has been reported to be the yield strain in compression for bone of different species (Bayraktar et al., 2004). The critical strain level was also varied in the range of $\pm 40\%$ ($-6180 \mu\epsilon$, $-8240 \mu\epsilon$, $-10300 \mu\epsilon$, $-12360 \mu\epsilon$ or $-14420 \mu\epsilon$).
- The tibia fails when a portion of the nodes (2%, 4%, 6%, 8% or 10%) reaches a critical tensile (first principal) strain of $8000 \mu\epsilon$, which has been reported to be the yield strain in tension for bone of different species (Bayraktar et al., 2004). The critical strain level was also varied in the range of $\pm 40\%$ ($4800 \mu\epsilon$, $6400 \mu\epsilon$, $8000 \mu\epsilon$, $9600 \mu\epsilon$ or $11200 \mu\epsilon$).
- The tibia fails when a portion of the nodes (2%, 4%, 6%, 8% or 10%) reaches a critical strain, either in tension (first principal strain of $6400 \mu\epsilon$) or in compression (third principal strain of $-14420 \mu\epsilon$), based on the optimal values from the analyses above.
- The tibia fails when the median first principal strain or third principal strain in one section (tibia divided into ten portions) or in one sector (tibia divided into ten sections and each section divided into anterior and posterior partitions; 20 portions in total) reaches $6400 \mu\epsilon$.

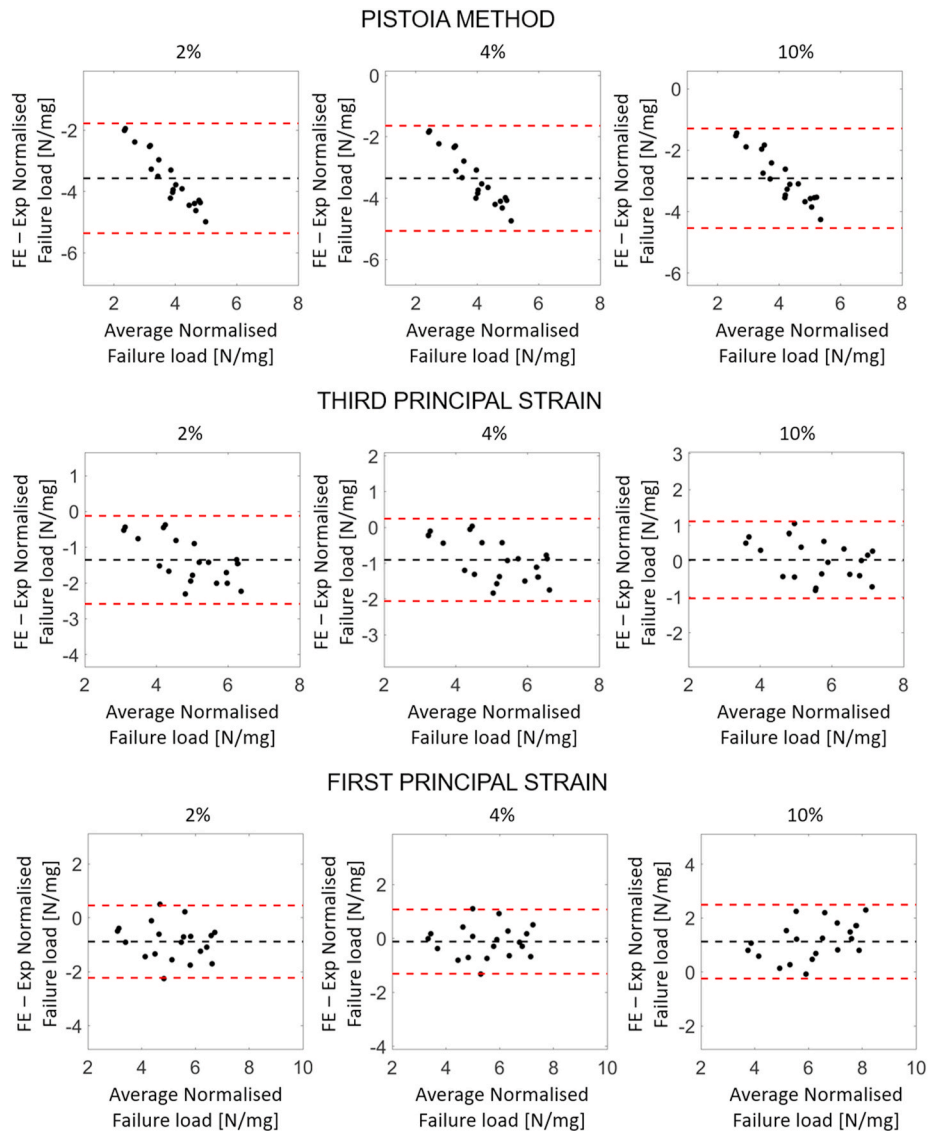


Fig. 6. Bland-Altman plots between the experimental measurements and microFE predictions of failure load based on different failure criteria (Pistoia method, third principal strain with critical strain level of $-14420 \mu\epsilon$, first principal strain with critical strain level of $6400 \mu\epsilon$). For each criterion the results for three failure volume levels are reported (2%, 4% and 10%). Normalized failure load was obtained by dividing by the total bone mineral content (BMC, [mg]).

$\mu\epsilon$ or $-14420 \mu\epsilon$ (optimal values for the global strain analyses), respectively. Details about the methods and the results for these criteria are reported in the [Appendix A](#).

2.7. Statistical analysis

Linear regression analysis was used to compare the experimental and predicted mechanical properties, as well as to assess if any morphometric or densitometric parameters could predict the measured stiffness or failure load. For each parameter, the following regression parameters were reported: slope and intercept of the regression line, coefficient of determination (R^2), root mean square error (RMSE), percentage error (mean and standard deviation). Statistical significance was defined at $p = 0.05$. For each regression (between experimental and microFE structural properties), the two-tailed Student's t-distribution (T.DIST.2T function, Excel) was used to determine if slope and intercept of the regression line were significantly different from 1 and 0 respectively. Statistical significance was defined at $p = 0.05$.

Multivariate regression analyses (IBM SPSS Statistics 25) were used to investigate sets of parameters that may predict the whole bone

stiffness and failure load. Two models were investigated. In the first model, morphometric measurements were included as independent variables (trabecular parameters, cortical thickness and total cross-sectional area). After checking for multicollinearity, trabecular number was excluded from the model, as it was strongly correlated with trabecular bone volume fraction ($R = 0.942$) and trabecular separation ($R = 0.885$). In the second model, BMC and second moments of area were added to the above-mentioned morphometric parameters as independent variables. I_{yy} and I_{zz} were excluded from the model, being strongly correlated with total cross-sectional area ($R = 0.923$) and I_{xx} ($R = 0.926$), respectively.

3. Results

All details about the correlations between bone mechanical properties and the morphometric or densitometric properties computed from the microCT images or the predicted structural properties estimated from microFE models are reported in [Appendix A](#). The reader is asked to refer to this appendix for p-values in case of significant correlations.

All microFE models took 30–40 min to solve (HPC ShARC, University

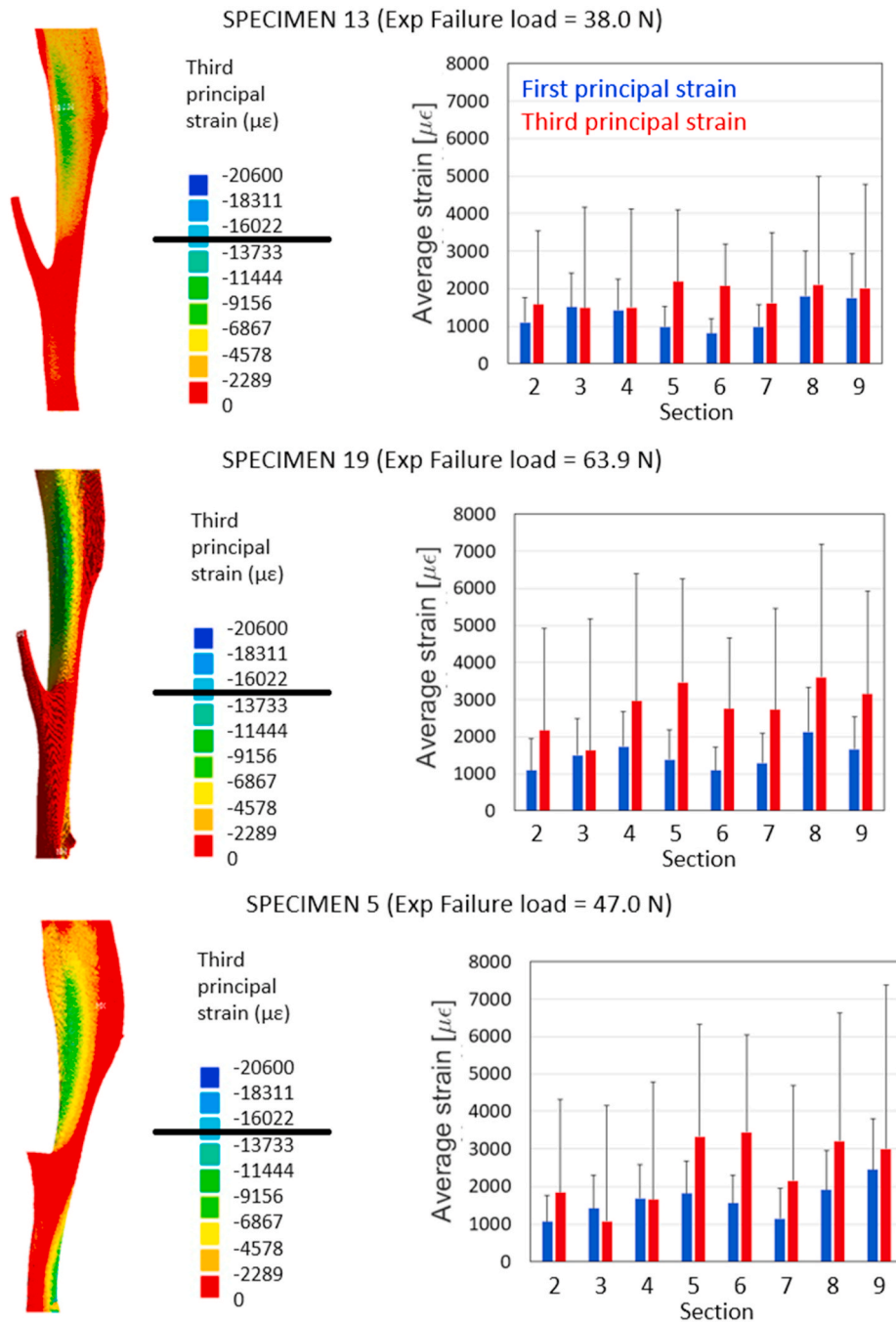


Fig. 7. Strain distributions for three specimens, for which the highest, lowest and average failure load was measured respectively. Section 1 = proximal tibia, section 10 = distal tibia. The black bar in the legend indicates the failure strain level assumed in the optimized failure criterion.

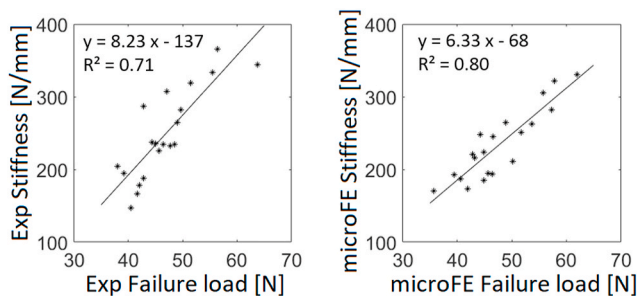


Fig. 8. Regression analysis between stiffness and failure load for experimental tests and microFE models.

of Sheffield; 8 cores, memory = 32GB/core). The tibia stiffness was best predicted by microFE models, while weak or no correlations were found with other parameters. Stiffness was weakly correlated with BV/TV in section 1 (proximal tibia, $R^2 = 0.20$) and with second moment of area in the medio-lateral direction in section 8 (distal tibia, $R^2 = 0.22$). No correlation was found between stiffness and any of the other morphometric or densitometric parameters ($p > 0.06$).

Normalized stiffness was weakly or moderately correlated with total TMD ($R^2 = 0.38$), total bone volume ($R^2 = 0.38$), BMC in the longitudinal sections ($R^2 = 0.38-0.61$) and sectors ($R^2 = 0.26-0.60$), and TMD in the longitudinal sections ($R^2 = 0.28-0.48$). A few weak correlations were also found for average total area in some longitudinal sections ($R^2 = 0.30$ for section 1 and 10), bone area ($R^2 = 0.28-0.29$ for sections 1, 7

and 10), second moment of area in the antero-posterior direction ($R^2 = 0.37$ – 0.46 for sections 1, 9 and 10) or in the medio-lateral direction ($R^2 = 0.32$ for section 8), and polar moment of inertia ($R^2 = 0.20$ – 0.36 for section 1, 9 and 10). Lastly, normalized stiffness was weakly correlated with trabecular thickness ($R^2 = 0.24$).

Experimental and microFE predictions of structural stiffness were well correlated ($R^2 = 0.65$; slope = 1.02 not significantly different from 1, $p = 0.89$; intercept = 9 N/mm not significantly different from 0, $p = 0.83$, Fig. 2). An excellent correlation was found between predicted and experimentally measured stiffness normalized by total BMC ($R^2 = 0.80$; slope = 1.20 not significantly different from 1, $p = 0.18$; intercept = -3 N/mm/mg not significantly different from 0, $p = 0.42$, Fig. 2). Absolute errors in the prediction of stiffness and normalized stiffness were $14\% \pm 8\%$. Errors were comparable across the stiffness magnitude range (Fig. 2).

Multiple regression models did not improve the prediction of stiffness. Stiffness could not be predicted by morphometric parameters ($p = 0.280$), nor by adding BMC and second moments of area to the model ($p = 0.116$).

Similar to the results obtained for stiffness, only weak correlations were observed between failure load and a few morphometric or densitometric parameters. Failure load was weakly correlated with average bone area ($R^2 = 0.25$), second moment of area in the antero-posterior direction ($R^2 = 0.37$) and polar moment of inertia ($R^2 = 0.35$) calculated in section 6 (tibial diaphysis). Failure load was also weakly correlated with second moment of area in the medio-lateral direction ($R^2 = 0.25$) calculated in section 9 weak correlation was found for total BV/TV ($R^2 = 0.33$) in section 1 (proximal tibia). No correlation was found between the other morphometric or densitometric parameters and failure load ($p > 0.05$).

Normalized failure load was moderately or well correlated with total TMD ($R^2 = 0.49$), total bone volume ($R^2 = 0.53$), BMC in the longitudinal sections ($R^2 = 0.50$ – 0.79) and sectors ($R^2 = 0.21$ – 0.79), TMD in the longitudinal sections ($R^2 = 0.33$ – 0.62). In particular, the highest correlations were found for BMC values in the lateral ($R^2 = 0.79$) and posterior ($R^2 = 0.77$) sectors of section 1 (proximal tibia) and in the medial sector of section 7 (distal tibia, $R^2 = 0.77$). A few weak or moderate correlations were also found for average total area in some longitudinal sections ($R^2 = 0.29$ – 0.45 for section 1, 9 and 10), bone area ($R^2 = 0.26$ – 0.41 for sections 1, 7, 9 and 10), second moment of area in the antero-posterior direction ($R^2 = 0.50$ – 0.59 for sections 1, 9 and 10), in the medio-lateral direction ($R^2 = 0.20$ – 0.22 for section 1 and 8) and polar moment of inertia ($R^2 = 0.35$ – 0.47 for section 1, 9 and 10). Lastly, normalized failure load was weakly correlated with cortical thickness ($R^2 = 0.22$).

Regression analyses between the experimental measurements and microFE predictions of failure load based on different failure criteria are reported in Fig. 3, while regression analyses for normalized failure load are reported in Fig. 4. In Figs. 5 and 6, Bland-Altman plots are reported for failure load and normalized failure load respectively. Failure load calculated using the Pistoia method dramatically underestimated the experimental measurement (slope = 1.74, intercept = 17N, absolute error = $63\% \pm 4\%$, Fig. 3). Also, prediction errors were dependent on the failure load magnitude (Figs. 5 and 6). The best correlation and lowest errors with respect to the experimental measurements were obtained by using the failure criterion based on third principal strain, a critical strain level equal to $-14420 \mu\epsilon$ and a failure volume of 10% ($R^2 = 0.48$ for failure load, slope = 0.64, intercept = 16N, absolute error = $9\% \pm 6\%$; $R^2 = 0.81$ for normalized failure load, slope = 1.07 not significantly different from 1, $p = 0.56$, intercept = 0 N/mg not significantly different from 0, $p = 0.54$, absolute error = $9\% \pm 6\%$, Figs. 3 and 4). Increasing the failure strain was associated with a decrease in slope of the regression line (from 1.93 to 0.64 for third principal strain of $-6180 \mu\epsilon$ to $-14420 \mu\epsilon$ and failed volume of 10%) and average error (from 56% to 9%). Similarly, an increase in failure volume was associated with a decrease in the slope of the regression line (from 0.83 to 0.64

for third principal strain of $-14420 \mu\epsilon$, Fig. 3) and in the average error (from 23% to 9%). The failure criterion based on combined first and principal strains did not improve the estimations. Since above 96% of nodes failed in compression first, results were similar to those obtained for third principal strain.

Strain distributions for three specimens (lowest, highest and average measured failure load) are reported in Fig. 7, as well as the average strains in each of the ten longitudinal sections. Spatial distributions of strains were similar among specimens, with peaks of compressive strain located at the postero-lateral apex and on the antero-medial surface towards the distal end of the tibia (Fig. 7).

Multiple regression models showed that failure load could not be predicted by morphometric parameters alone ($p = 0.437$). By adding BMC and second moments of area, the model was able to predict failure load ($R^2 = 0.714$, $p = 0.014$). Details of the regression parameters are reported in the Appendix (Table A9). It should be noticed that the only parameters that contributed significantly to the regression model were BMC ($p = 0.012$) and I_{xx} ($p = 0.002$).

Regression analyses between stiffness and failure load showed very good correlation for both experimental tests ($R^2 = 0.71$) and FE predictions ($R^2 = 0.80$) (Fig. 8).

4. Discussion

In this study, the best predictors of experimentally measured structural mechanical properties of the mouse tibia among morphometric and densitometric properties, measured from *in vivo* microCT, and structural properties predicted from microCT-based microFE models, have been investigated. Moreover, the failure criterion for microFE models of the mouse tibia in compression has been optimized for the first time.

Structural properties measured under compression were only weakly correlated with geometrical properties. This is in contrast with what was observed for bending tests, where the experimental failure load was strongly correlated with the moment of inertia at the midshaft ($R^2 = 0.84$) (Varga et al., 2020), highlighting the dependence on the different loading condition (four-point bending test vs apparent compression applied in this study). Nevertheless, it is interesting to notice that the failure load measured in compression was weakly correlated with cross-sectional moments of inertia at the midshaft and below the tibio-fibular junction ($R^2 = 0.25$ – 0.37), which correspond to the locations of peak strains (Fig. 7). Structural properties were not correlated with total bone mineral content or with local tissue mineral density in the longitudinal sections, which suggests that the geometry and loading conditions are the main drivers determining the measured structural properties. However, it should be noted that BMC in a few sections (section 1 and 7) or sectors (postero-lateral sectors at the proximal tibia, or medial sector at the distal tibia) of the bone showed very good correlation with normalized failure load ($R^2 = 0.77$ – 0.79), which is similar to the predictions from microFE models ($R^2 = 0.81$). Similarly, failure load could be predicted ($R^2 = 0.71$) using a combination of densitometric (total BMC) and geometric (second moment of area along the antero-posterior axis) parameters. While this result highlights that BMC in a specific region of the tibia, or a combination of multiple parameters, can be used to estimate its normalized failure load, it should be noted that this is valid only for this specific loading scenario, while the microFE models can potentially provide an estimate of the mechanical properties in different loading conditions after proper validation.

The correlations found in this study between experimental and microFE predicted structural properties were generally lower compared to previous validation studies on different mouse bone structures ($R^2 = 0.62$ – 0.89 for the mouse vertebra in compression (Nyman et al., 2015), $R^2 = 0.93$ for the mouse femur in four-point bending (Varga et al., 2020)). This difference may be due to the simpler geometry of the vertebral body compared to the tibia and considering that in four-point bending tests the mechanical properties are mainly driven by the small portion of bone between the loading pins. Due to the higher aspect ratio

and the natural curvature of the tibia, when it is nominally loaded in compression along the longitudinal direction its tissue is subjected to a complex combination of compression and bending. We cannot exclude that a small misalignment between the direction of the experimental load and the load applied in the models may have a greater impact on the overall loading scenario, compared to the compression of shorter bones (vertebral body) or the four-point bending test. In order to minimize these differences, we acquired the microCT images after embedding the tibia extremities in resin, so that the embedding material provided the reference surface for identifying the direction of the applied displacement. The model predictions improved for structural mechanical properties normalized by total bone mineral content (BMC). This suggests that the variability in the size and mineral density of the specimens could have an effect on the model accuracy by leading to a larger scatter in the model predictions, which are compensated by the BMC normalization.

The failure criterion developed by Pistoia et al. (2002) for the human distal radius had to be adapted for its application to the mouse tibia. Errors of $9\% \pm 6\%$ were obtained by assuming that the tibia fails when 10% of the nodes reach a third principal strain of $-14420 \mu\epsilon$. This was in line with the findings of previous phenomenological models, showing that the failure criterion had to be tuned according to the specific bone structure and analyzed loading scenario. In compression, a criterion based on third principal strain performed better than one based on effective strain, suggesting that the majority of the nodes failed in compression. The larger failure volume (10%) indicates greater resistance of the structure in compression compared to bending. It should be noted that the predictions based on the effective strain led to large errors with regression slopes far from 1 and a proportional bias as shown by the Bland-Altman plots, highlighting that this approach is not ideal for the mouse tibia. In Varga et al. (2020), the optimized parameters for predicting the failure load of the mouse femur in four-point bending were failure volume of 3% and critical strain of $10000 \mu\epsilon$. For the mouse vertebra, it was shown that the optimized parameters were dependant on the assigned material properties (Nyman et al., 2015). Lastly, in a previous study using time-lapsed compression and digital volume correlation analyses by our group (Oliviero et al., 2018), it was shown that a failure volume of 2% and critical strain of $-10300 \mu\epsilon$ led to errors of $9\% \pm 9\%$ for the prediction of mouse tibia failure load. This difference in the optimal failure criterion parameters was likely due to the difference in the experimental testing modality. Nevertheless, in this study the experimental and predicted normalized failure load were very well correlated ($R^2 = 0.81$ for failure load divided by the total bone mineral content) with low absolute errors ($9\% \pm 6\%$).

This study has some limitations. First, the microFE models used for the predictions of the mechanical properties are relatively simple, with hexahedral meshes and homogeneous material properties. Differences in local TMD and Young's modulus were not modelled and could lead to a different strain distribution and, therefore, to a different value of predicted stiffness and strength. Nevertheless, the good quantitative predictions of structural stiffness suggest that the considered elastic modulus was reasonable. Moreover, homogeneous models based on hexahedral mesh can be very useful for application in longitudinal studies, as they require minimal pre-processing, operator interactions,

and reasonable computation time. Furthermore, in a previous study we have shown that these models can accurately predict the local displacements over the tibia volume in compression (Oliviero et al., 2018), confirming the models accuracy for local predictions, important for bone remodeling algorithms (Cheong et al., 2020), and normalized structural properties. Also, boundary conditions were defined by assuming that the displacement applied to the top surface of the embedding material was perfectly transmitted to the top surface of the tibia free length. While this approach should minimize the differences between experiments and computational models, any compliance in the embedding material or in the fixation device of the machine was not accounted for, which could explain lower correction for stiffness. Another limitation of this study was the relatively small range of properties of the tested tibiae. In order to increase the range in mechanical properties, tibiae from different groups of mice were included in the study. Nevertheless, a larger age range may have increased the variability in bone mechanical properties due to differences in micro-structure, nano-porosities and mineral density distribution. Lastly, while the failure criterion has been calibrated for the reported dataset, in order to generalize the findings, the developed approach should be validated in the future using an independent group of specimens, possibly extending the age range and adding other inbred mouse strains.

In conclusion, an optimal failure criterion was identified for predicting the failure load of the mouse tibia from linear microFE models generated from *in vivo* microCT images. These models can be applied in longitudinal preclinical studies for the non-invasive prediction of the structural mechanical properties of the mouse tibia.

CRediT authorship contribution statement

S. Oliviero: Conceptualization, Methodology, Software, Validation, Formal analysis, Investigation, Data curation, Writing - original draft. **R. Owen:** Methodology, Investigation, Data curation, Writing - review & editing. **G.C. Reilly:** Visualization, Resources, Writing - review & editing. **I. Bellantuono:** Conceptualization, Funding acquisition, Writing - review & editing. **E. Dall'Ara:** Conceptualization, Data curation, Resources, Supervision, Project administration, Funding acquisition, Writing - review & editing.

Declaration of competing interest

The authors declare that they have no known competing financial interests or personal relationships that could have appeared to influence the work reported in this paper.

Acknowledgements

The study was partially funded by the UK National Centre for the Replacement, Refinement and Reduction of Animals in Research (NC3Rs), Grant number: NC/R001073/1) and by the Engineering and Physical Sciences Research Council (EPSRC) Frontier Multisim Grant (EP/K03877X/1 and EP/S032940/1). RO was funded by an EPSRC Doctoral Prize Fellowship (EP/N509735/1). The authors acknowledge the Skeletal laboratory for the access to the imaging facilities.

Appendices.

Appendix A. Detailed statistics for the morphometric, densitometric and microFE predicted mechanical predictors of experimentally measured mechanical properties

Table A1

Regression parameters for the different failure criteria analyzed. For every regression p-value < 0.001. * indicates that the Slope was not significantly different from 1 (p-value>0.05). ** indicates that the Intercept was not significantly different from 0 (p-value>0.05).

Failure volume	Failure strain [$\mu\epsilon$]	R ²	Slope	Int [N]	RMSE [N]	Mean Error [%]	SD Error [%]
2%	7000	0.53	1.74*	17	4.49	63	4
4%	7000	0.52	1.59*	17	4.51	60	4
10%	7000	0.49	1.34*	16	4.67	51	5
2%	-6180	0.52	1.93	17	4.50	67	4
4%	-6180	0.52	1.77*	17	4.53	64	4
10%	-6180	0.48	1.50*	16	4.69	56	5
2%	-8240	0.52	1.45*	17	4.50	56	5
4%	-8240	0.52	1.33*	17	4.53	52	5
10%	-8240	0.48	1.12*	16	4.69	42	6
2%	-10300	0.52	1.16*	17	4.50	45	6
4%	-10300	0.52	1.06*	17	4.53	39	7
10%	-10300	0.48	0.90*	16	4.69	27	8
2%	-12360	0.52	0.97*	17	4.50	34	7
4%	-12360	0.52	0.89*	17	4.53	27	8
10%	-12360	0.48	0.75*	16	4.69	13	8
2%	-14420	0.52	0.83*	17	4.50	23	8
4%	-14420	0.52	0.76*	17	4.53	15	9
10%	-14420	0.48	0.64	16	4.69	9	6
2%	4800	0.62	0.77*	24	4.02	37	9
4%	4800	0.66	0.76*	21	3.82	26	9
10%	4800	0.63	0.65	19	3.95	11	8
2%	6400	0.62	0.58	24	4.02	17	9
4%	6400	0.66	0.57	21	3.82	9	7
10%	6400	0.63	0.49	19	3.95	21	13
2%	8000	0.62	0.46	24	4.02	12	9
4%	8000	0.66	0.45	21	3.82	23	14
10%	8000	0.63	0.39	19	3.95	51	17
2%	9600	0.62	0.38	24	4.02	28	16
4%	9600	0.66	0.38	21	3.82	48	17
10%	9600	0.63	0.33	19	3.95	81	20
2%	11200	0.62	0.33	24	4.02	48	20
4%	11200	0.66	0.32	21	3.82	72	20
10%	11200	0.63	0.28	19	3.95	111	23
2%	Combined	0.54	0.77*	21	4.44	28	9
4%	Combined	0.55	0.73*	20	4.35	20	9
10%	Combined	0.56	0.65	18	4.31	9	7

Regression parameters and absolute errors for failure load predicted using different failure criteria are reported in [Table A1](#).

Table A2

Regression parameters for the different failure criteria analyzed. For every regression p-value < 0.001. * indicates that the Slope was not significantly different from 1 (p-value>0.05). ** indicates that the Intercept was not significantly different from 0 (p-value>0.05).

Failure volume	Failure strain [$\mu\epsilon$]	R ²	Slope	Int [N/mg]	RMSE [N/mg]	Mean Error [%]	SD Error [%]
2%	7000	0.80	2.82	0**	0.58	63	4
4%	7000	0.80	2.52	0**	0.57	60	4
10%	7000	0.81	2.25	0**	0.56	51	5
2%	-6180	0.80	3.10	0**	0.58	67	4
4%	-6180	0.80	2.80	0**	0.57	64	4
10%	-6180	0.81	2.50	0**	0.56	56	5
2%	-8240	0.80	2.32	0**	0.58	56	5
4%	-8240	0.80	2.10	0**	0.57	52	5
10%	-8240	0.81	1.88	0**	0.56	42	6
2%	-10300	0.80	1.86	0**	0.58	45	6
4%	-10300	0.80	1.68	0**	0.57	39	7
10%	-10300	0.81	1.50	0**	0.56	27	8
2%	-12360	0.80	1.55	0**	0.58	34	7
4%	-12360	0.80	1.40	0**	0.57	27	8
10%	-12360	0.81	1.25*	0**	0.56	13	8
2%	-14420	0.80	1.33	0**	0.58	23	8
4%	-14420	0.80	1.20*	0**	0.57	15	9
10%	-14420	0.81	1.07*	0**	0.56	9	6
2%	4800	0.70	1.23*	1**	0.70	37	9

(continued on next page)

Table A2 (continued)

Failure volume	Failure strain [$\mu\epsilon$]	R ²	Slope	Int [N/mg]	RMSE [N/mg]	Mean Error [%]	SD Error [%]
4%	4800	0.78	1.16*	1**	0.60	26	9
10%	4800	0.80	0.97*	1**	0.58	11	8
2%	6400	0.70	0.93*	1**	0.70	17	9
4%	6400	0.78	0.87*	1**	0.60	9	7
10%	6400	0.80	0.73	1**	0.58	21	13
2%	8000	0.70	0.74	1**	0.70	12	9
4%	8000	0.78	0.70	1**	0.60	23	14
10%	8000	0.80	0.58	1**	0.58	51	17
2%	9600	0.70	0.62	1**	0.70	28	16
4%	9600	0.78	0.58	1**	0.60	48	17
10%	9600	0.80	0.49	1**	0.58	81	20
2%	11200	0.70	0.53	1**	0.70	48	20
4%	11200	0.78	0.50	1**	0.60	72	20
10%	11200	0.80	0.42	1**	0.58	111	23
2%	Combined	0.74	1.27*	1**	0.66	28	9
4%	Combined	0.77	1.14*	1**	0.62	20	9
10%	Combined	0.79	1.01*	0**	0.58	9	7

Regression parameters and absolute errors for normalized failure load predicted using different failure criteria are reported in [Table A2](#).

Two additional failure criteria were tested, based on strains spatially localized in critical regions of the bone:

- The tibia was divided into 10 longitudinal sections and it was assumed that the tibia fails when the median first principal strain in one section reaches 6400 $\mu\epsilon$, or the median third principal strain in one section reaches -14420 $\mu\epsilon$ (optimal values for the global strain analyses), or when the first among the two limits in tension or compression is reached.
- The tibia was divided into 10 longitudinal sections, and in the antero-posterior direction according to the centroid of each cross-section (20 partitions in total). It was assumed that the tibia fails when the median first principal strain in one region reaches 6400 $\mu\epsilon$, or the median third principal strain in one region reaches -14420 $\mu\epsilon$ (optimal values for the global strain analyses), or when the first among the two limits in tension or compression is reached.

Table A3

Regression parameters for the different failure criteria analyzed. The tibia was divided into either 10 regions of interest (10 longitudinal sections) or 20 regions of interest (10 longitudinal sections, each divided into an anterior and a posterior partition). For every regression p-value < 0.001.

Region of interest	Strain Criterion	R ²	Slope	Int [N]	RMSE [N]	Mean Error [%]	SD Error [%]
10 sections	First Principal	0.47	0.29	27	4.74	44	23
10 sections	Third Principal	0.05	0.10	36	6.37	149	41
10 sections	Combined	0.42	0.33	28	4.98	23	18
20 A or P partitions	First Principal	0.44	0.42	22	4.86	28	16
20 A or P Partitions	Third principal	0.27	0.43	27	5.58	12	12
20 A or P partitions	Combined	0.42	0.58	20	4.99	11	8

These failure criteria based on dividing the tibia into partitions did not improve the estimation of strength (R² = 0.05–0.47, slope = 0.10–0.58). Regression parameters and absolute errors are reported in [Table A3](#).

Table A4

Regression parameters for the different failure criteria analyzed. The tibia was divided into either 10 regions of interest (10 longitudinal sections) or 20 regions of interest (10 longitudinal sections, each divided into an anterior and a posterior partition). For every regression p-value < 0.001. * indicates that the Slope was not significantly different from 1 (p-value>0.05). ** indicates that the Intercept was not significantly different from 0 (p-value>0.05).

Region of interest	Strain Criterion	R ²	Slope	Int [N/mg]	RMSE [N/mg]	Mean Error [%]	SD Error [%]
10 sections	First Principal	0.58	0.59	1**	0.83	44	23
10 sections	Third Principal	0.58	0.53	-2**	0.83	149	41
10 sections	Combined	0.53	0.65	1**	0.87	23	18
20 A or P partitions	First Principal	0.72	0.83*	0**	0.68	28	16
20 A or P Partitions	Third principal	0.69	1.19*	-1**	0.71	12	12
20 A or P partitions	Combined	0.79	1.25*	-1**	0.59	11	8

Regression parameters and errors for normalized failure load predicted by dividing the tibia into partitions are reported in [Table A4](#).

Table A5

Regression parameters for the different predictors of stiffness. BV/TV = bone volume fraction; I_{yy} = second moment of area in medio-lateral direction.

Predictor	Region of interest	R ²	Slope	Intercept [N/mm]	RMSE [N/mm]	P value
BV/TV	Section 1	0.20	548.64	-30	56.91	0.045
I_{yy}	Section 8	0.22	3375.49	81	56.37	0.037

Regression parameters and errors for stiffness predicted using different morphometric and densitometric parameters are reported in [Table A5](#).

Table A6

Regression parameters for the different predictors of failure load. BV/TV = bone volume fraction; I_{xx} = second moment of area in antero-posterior direction; I_{yy} = second moment of area in medio-lateral direction; I_{zz} = second moment of area in longitudinal direction.

Predictor	Region of interest	R ²	Slope	Intercept [N]	RMSE [N]	P value
BV/TV	Section 1	0.33	71.56	10	5.33	0.008
Bone area	Section 6	0.25	47.84	20	5.67	0.026
I_{xx}	Section 6	0.37	190.75	34	5.17	0.004
I_{zz}	Section 6	0.35	139.56	31	5.26	0.006
I_{yy}	Section 9	0.25	465.70	27	5.67	0.026

Regression parameters and errors for failure load predicted using different morphometric and densitometric parameters are reported in [Table A6](#).

Table A7

Regression parameters for the different predictors of normalized stiffness. Tb.Th = trabecular thickness; BMC = bone mineral content; TMD = tissue mineral density; BV = bone volume; TV = total volume; BV/TV = bone volume fraction; BMD = bone mineral density; I_{xx} = second moment of area in antero-posterior direction; I_{yy} = second moment of area in medio-lateral direction; I_{zz} = second moment of area in longitudinal direction.

Predictor	Region of interest	R ²	Slope	Intercept [N/mm/mg]	RMSE [N/mm/mg]	P value
Tb.Th	Trabecular ROI	0.24	-1.13	91	8.91	0.029
BMC	Total tibia	0.53	-4.06	65	6.99	<0.001
TMD	Total tibia	0.38	-0.08	103	8.02	0.004
BV	Total tibia	0.38	-4.21	69	8.06	0.004
TV	Total tibia	0.27	-2.27	63	8.73	0.019
BMD	Total tibia	0.21	-0.05	61	9.07	0.041
BMC	Section 1	0.61	-31.02	65	6.36	<0.001
TMD	Section 1	0.35	-0.07	100	8.22	0.006
BV	Section 1	0.48	-32.58	69	7.38	0.001
TV	Section 1	0.44	-11.24	57	7.64	0.001
Total area	Section 1	0.30	-17.60	60	8.55	0.012
Bone area	Section 1	0.28	-54.15	77	8.67	0.016
I_{xx}	Section 1	0.46	-76.73	47	7.52	0.001
I_{zz}	Section 1	0.36	-42.90	50	8.19	0.005
BMC	Section 2	0.55	-39.58	70	6.82	<0.001
TMD	Section 2	0.36	-0.07	99	8.21	0.006
BV	Section 2	0.29	-31.20	63	8.63	0.015
BMD	Section 2	0.21	-0.06	61	9.07	0.041
BMC	Section 3	0.49	-43.25	70	7.31	0.001
TMD	Section 3	0.36	-0.07	93	8.21	0.006
BV	Section 3	0.20	-31.45	61	9.14	0.048
BMD	Section 3	0.23	-0.05	58	8.98	0.033
BMC	Section 4	0.44	-43.68	68	7.65	0.001
TMD	Section 4	0.35	-0.07	97	8.23	0.006
BMD	Section 4	0.23	-0.05	60	8.98	0.033
BMC	Section 5	0.44	-46.18	66	7.66	0.001
TMD	Section 5	0.32	-0.06	91	8.46	0.010
BV	Section 5	0.23	-39.09	62	8.98	0.033
BMD	Section 5	0.28	-0.05	60	8.66	0.016
BMC	Section 6	0.47	-38.27	59	7.42	0.001
TMD	Section 6	0.48	-0.07	101	7.35	0.001
BV	Section 6	0.32	-41.19	62	8.43	0.009
BMD	Section 6	0.42	-0.05	64	7.78	0.002
BV/TV	Section 6	0.22	-61.63	72	9.02	0.036
BMC	Section 7	0.59	-39.85	66	6.55	<0.001
TMD	Section 7	0.40	-0.08	109	7.94	0.003
BV	Section 7	0.49	-45.52	73	7.33	0.001
TV	Section 7	0.33	-33.65	72	8.34	0.008
BMD	Section 7	0.36	-0.06	73	8.15	0.005
Bone area	Section 7	0.28	-79.16	84	8.66	0.016
BMC	Section 8	0.38	-45.04	65	8.04	0.004
TMD	Section 8	0.28	-0.07	92	8.64	0.015
BV	Section 8	0.23	-44.82	67	8.96	0.032
I_{yy}	Section 8	0.32	652.82	-3	8.43	0.009
BMC	Section 9	0.45	-38.74	57	7.58	0.001
TMD	Section 9	0.37	-0.08	99	8.11	0.004
BV	Section 9	0.37	-43.09	63	8.10	0.004
TV	Section 9	0.39	-39.12	73	7.98	0.003

(continued on next page)

Table A7 (continued)

Predictor	Region of interest	R ²	Slope	Intercept [N/mm/mg]	RMSE [N/mm/mg]	P value
BMD	Section 9	0.24	-0.05	63	8.91	0.028
Ixx	Section 9	0.37	-535.42	58	8.10	0.004
Izz	Section 9	0.20	-273.23	56	9.13	0.047
BMC	Section 10	0.42	-21.72	49	7.81	0.002
TMD	Section 10	0.35	-0.07	95	8.24	0.006
BV	Section 10	0.38	-24.16	53	8.07	0.004
TV	Section 10	0.39	-19.30	56	7.95	0.003
BMD	Section 10	0.23	-0.06	67	8.96	0.032
Total area	Section 10	0.30	-33.02	62	8.57	0.013
Bone area	Section 10	0.29	-39.80	57	8.63	0.015
Ixx	Section 10	0.44	-152.63	46	7.63	0.001
Izz	Section 10	0.29	-76.11	42	8.64	0.015
BMC	Sec 1 Lateral	0.58	-84.42	57	6.64	<0.001
BMC	Sec 1 Anterior	0.56	-144.31	73	6.80	<0.001
BMC	Sec 1 Medial	0.52	-156.14	65	7.06	<0.001
BMC	Sec 1 Posterior	0.60	-105.82	60	6.45	<0.001
BMC	Sec 2 Lateral	0.43	-110.99	59	7.69	0.002
BMC	Sec 2 Anterior	0.56	-164.93	79	6.77	<0.001
BMC	Sec 2 Medial	0.50	-192.57	65	7.21	<0.001
BMC	Sec 2 Posterior	0.57	-140.36	68	6.67	<0.001
BMC	Sec 3 Lateral	0.37	-110.98	56	8.10	0.004
BMC	Sec 3 Anterior	0.47	-172.87	81	7.46	0.001
BMC	Sec 3 Medial	0.39	-236.68	65	7.95	0.003
BMC	Sec 3 Posterior	0.53	-147.92	68	7.03	<0.001
BMC	Sec 4 Lateral	0.40	-122.80	57	7.88	0.003
BMC	Sec 4 Anterior	0.26	-127.44	64	8.82	0.023
BMC	Sec 4 Medial	0.32	-176.99	57	8.45	0.010
BMC	Sec 4 Posterior	0.41	-139.04	62	7.83	0.002
BMC	Sec 5 Lateral	0.47	-135.19	59	7.44	0.001
BMC	Sec 5 Medial	0.34	-136.23	54	8.33	0.007
BMC	Sec 5 Posterior	0.41	-179.38	65	7.84	0.002
BMC	Sec 6 Lateral	0.48	-113.81	54	7.35	0.001
BMC	Sec 6 Anterior	0.28	-135.40	53	8.66	0.016
BMC	Sec 6 Medial	0.41	-120.98	54	7.83	0.002
BMC	Sec 6 Posterior	0.39	-150.15	56	7.96	0.003
BMC	Sec 7 Lateral	0.53	-87.95	53	6.98	<0.001
BMC	Sec 7 Anterior	0.42	-155.51	60	7.77	0.002
BMC	Sec 7 Medial	0.56	-119.20	59	6.79	<0.001
BMC	Sec 8 Lateral	0.30	-127.19	55	8.55	0.012
BMC	Sec 8 Anterior	0.39	-175.27	62	7.97	0.003
BMC	Sec 8 Medial	0.34	-136.92	58	8.32	0.007
BMC	Sec 9 Lateral	0.53	-112.31	52	7.04	<0.001
BMC	Sec 9 Anterior	0.31	-152.95	54	8.47	0.010
BMC	Sec 9 Medial	0.33	-113.94	50	8.35	0.008
BMC	Sec 9 Posterior	0.36	-185.11	60	8.15	0.005
BMC	Sec 10 Lateral	0.47	-58.07	48	7.44	0.001
BMC	Sec 10 Anterior	0.39	-136.18	53	7.97	0.003
BMC	Sec 10 Medial	0.35	-65.34	45	8.21	0.006
BMC	Sec 10 Posterior	0.33	-116.99	50	8.40	0.009

Regression parameters and errors for normalized stiffness predicted using different morphometric and densitometric parameters are reported in Table A7.

Table A8

Regression parameters for the different predictors of normalized failure load. Ct.Th = cortical thickness; BMC = bone mineral content; TMD = tissue mineral density; BV = bone volume; TV = total volume; BV/TV = bone volume fraction; BMD = bone mineral density; Ixx = second moment of area in antero-posterior direction; Iyy = second moment of area in medio-lateral direction; Izz = second moment of area in longitudinal direction.

Predictor	Region of interest	R ²	Slope	Intercept [N/mg]	RMSE [N/mg]	P value
Ct.Th	Diaphysis	0.22	-0.02	10	1.13	0.035
BMC	Total tibia	0.73	-0.60	11	0.67	<0.001
TMD	Total tibia	0.49	-0.01	16	0.92	0.001
BV	Total tibia	0.53	-0.63	11	0.87	<0.001
TV	Total tibia	0.40	-0.35	11	0.99	0.003
BMD	Total tibia	0.25	-0.01	10	1.11	0.025
Bone area	Total tibia	0.24	-9.61	12	1.12	0.027
Minimum Bone Area	Total tibia	0.29	-13.39	13	1.08	0.014
BMC	Section 1	0.79	-4.41	11	0.59	<0.001
TMD	Section 1	0.42	-0.01	15	0.98	0.002
BV	Section 1	0.63	-4.68	11	0.78	<0.001
TV	Section 1	0.56	-1.59	9	0.85	<0.001
Total area	Section 1	0.40	-2.53	10	1.00	0.003
Bone area	Section 1	0.39	-8.00	13	1.00	0.003
Ixx	Section 1	0.59	-10.90	8	0.82	<0.001
Iyy	Section 1	0.20	-9.14	8	1.14	0.046

(continued on next page)

Table A8 (continued)

Predictor	Region of interest	R ²	Slope	Intercept [N/mg]	RMSE [N/mg]	P value
Izz	Section 1	0.47	-6.16	8	0.93	0.001
BMC	Section 2	0.76	-5.79	11	0.63	<0.001
TMD	Section 2	0.43	-0.01	15	0.96	0.002
BV	Section 2	0.41	-4.69	11	0.98	0.002
TV	Section 2	0.22	-1.76	9	1.13	0.035
BMD	Section 2	0.24	-0.01	10	1.12	0.030
BMC	Section 3	0.70	-6.50	12	0.70	<0.001
TMD	Section 3	0.45	-0.01	14	0.95	0.001
BV	Section 3	0.32	-4.98	11	1.06	0.010
BMD	Section 3	0.28	-0.01	9	1.09	0.017
BMC	Section 4	0.69	-6.86	12	0.71	<0.001
TMD	Section 4	0.48	-0.01	15	0.93	0.001
BV	Section 4	0.35	-5.67	11	1.04	0.006
BMD	Section 4	0.32	-0.01	10	1.06	0.010
BMC	Section 5	0.67	-7.14	11	0.74	<0.001
TMD	Section 5	0.43	-0.01	15	0.97	0.002
BV	Section 5	0.37	-6.23	11	1.02	0.005
BMD	Section 5	0.35	-0.01	10	1.03	0.006
BMC	Section 6	0.63	-5.56	10	0.78	<0.001
TMD	Section 6	0.62	-0.01	16	0.79	<0.001
BV	Section 6	0.43	-6.01	10	0.97	0.002
BMD	Section 6	0.48	-0.01	10	0.92	0.001
BV/TV	Section 6	0.21	-7.52	11	1.14	0.042
BMC	Section 7	0.79	-5.77	11	0.59	<0.001
TMD	Section 7	0.52	-0.01	17	0.89	<0.001
BV	Section 7	0.64	-6.56	12	0.77	<0.001
TV	Section 7	0.48	-5.07	12	0.92	0.001
BMD	Section 7	0.43	-0.01	11	0.97	0.002
Bone area	Section 7	0.39	-11.70	14	1.00	0.003
BMC	Section 8	0.50	-6.50	11	0.90	<0.001
TMD	Section 8	0.33	-0.01	14	1.05	0.008
BV	Section 8	0.33	-6.72	11	1.05	0.008
TV	Section 8	0.33	-5.86	12	1.05	0.008
BMD	Section 8	0.20	-0.01	10	1.15	0.050
Iyy	Section 8	0.22	67.92	2	1.13	0.037
BMC	Section 9	0.60	-5.63	10	0.81	<0.001
TMD	Section 9	0.48	-0.01	15	0.93	0.001
BV	Section 9	0.50	-6.29	10	0.90	<0.001
TV	Section 9	0.57	-5.94	12	0.84	<0.001
BMD	Section 9	0.28	-0.01	10	1.09	0.017
Total area	Section 9	0.29	-10.68	14	1.08	0.015
Bone area	Section 9	0.26	-9.57	11	1.10	0.021
Ixx	Section 9	0.50	-78.12	10	0.90	<0.001
Izz	Section 9	0.35	-45.15	10	1.03	0.006
BMC	Section 10	0.56	-3.16	8	0.85	<0.001
TMD	Section 10	0.45	-0.01	15	0.95	0.001
BV	Section 10	0.51	-3.53	9	0.90	<0.001
TV	Section 10	0.56	-2.87	9	0.86	<0.001
BMD	Section 10	0.26	-0.01	10	1.10	0.020
Total area	Section 10	0.45	-5.11	10	0.95	0.001
Bone area	Section 10	0.41	-5.93	10	0.99	0.003
Ixx	Section 10	0.56	-21.52	8	0.85	<0.001
Izz	Section 10	0.40	-11.30	7	0.99	0.003
BMC	Sec 1 Lateral	0.79	-12.33	10	0.59	<0.001
BMC	Sec 1 Anterior	0.74	-20.80	12	0.66	<0.001
BMC	Sec 1 Medial	0.58	-20.69	10	0.83	<0.001
BMC	Sec 1 Posterior	0.77	-15.05	10	0.61	<0.001
BMC	Sec 2 Lateral	0.65	-16.98	10	0.76	<0.001
BMC	Sec 2 Anterior	0.71	-23.27	12	0.69	<0.001
BMC	Sec 2 Medial	0.68	-28.12	11	0.72	<0.001
BMC	Sec 2 Posterior	0.77	-20.32	11	0.62	<0.001
BMC	Sec 3 Lateral	0.57	-17.16	10	0.84	<0.001
BMC	Sec 3 Anterior	0.63	-25.12	13	0.78	<0.001
BMC	Sec 3 Medial	0.60	-36.61	11	0.81	<0.001
BMC	Sec 3 Posterior	0.73	-21.83	11	0.67	<0.001
BMC	Sec 4 Lateral	0.59	-18.59	10	0.82	<0.001
BMC	Sec 4 Anterior	0.41	-20.22	11	0.99	0.002
BMC	Sec 4 Medial	0.54	-29.10	10	0.87	<0.001
BMC	Sec 4 Posterior	0.65	-21.94	11	0.75	<0.001
BMC	Sec 5 Lateral	0.64	-19.84	10	0.77	<0.001
BMC	Sec 5 Anterior	0.21	-14.79	9	1.14	0.045
BMC	Sec 5 Medial	0.53	-21.44	9	0.88	<0.001
BMC	Sec 5 Posterior	0.62	-27.49	11	0.79	<0.001
BMC	Sec 6 Lateral	0.58	-15.64	9	0.83	<0.001
BMC	Sec 6 Anterior	0.37	-19.35	9	1.02	0.005
BMC	Sec 6 Medial	0.61	-18.38	9	0.81	<0.001

(continued on next page)

Table A8 (continued)

Predictor	Region of interest	R ²	Slope	Intercept [N/mg]	RMSE [N/mg]	P value
BMC	Sec 6 Posterior	0.57	-22.68	10	0.84	<0.001
BMC	Sec 7 Lateral	0.64	-12.03	9	0.77	<0.001
BMC	Sec 7 Anterior	0.56	-22.42	10	0.85	<0.001
BMC	Sec 7 Medial	0.77	-17.54	10	0.62	<0.001
BMC	Sec 8 Lateral	0.37	-17.74	9	1.02	0.004
BMC	Sec 8 Anterior	0.50	-24.93	10	0.90	<0.001
BMC	Sec 8 Medial	0.46	-20.12	10	0.94	0.001
BMC	Sec 8 Posterior	0.25	-18.72	9	1.11	0.024
BMC	Sec 9 Lateral	0.66	-15.83	9	0.74	<0.001
BMC	Sec 9 Anterior	0.41	-21.88	9	0.99	0.002
BMC	Sec 9 Medial	0.46	-16.81	9	0.94	0.001
BMC	Sec 9 Posterior	0.56	-28.66	10	0.85	<0.001
BMC	Sec 10 Lateral	0.58	-8.12	8	0.83	<0.001
BMC	Sec 10 Anterior	0.55	-20.29	9	0.86	<0.001
BMC	Sec 10 Medial	0.49	-9.67	8	0.91	0.001
BMC	Sec 10 Posterior	0.49	-17.94	9	0.92	0.001

Regression parameters and errors for normalized failure load predicted using different morphometric and densitometric parameters are reported in Table A8.

Table A9

Coefficients and p values for each independent variable in the model.

	Coefficients	p
Constant	14.059	0.491
Tb.BV/TV	0.678	0.558
Tb.Th	-0.150	0.750
Tb.Sp	0.041	0.372
Ct.Th	0.116	0.078
Tt.Ar	4.982	0.639
BMC	-3.024	0.012
Ixx	255.602	0.002

Regression parameters for failure load predicted by multivariate model ($R^2 = 0.714$, $p = 0.014$) are reported in Table A9. Seven independent variables were included: trabecular bone volume fraction, thickness and separation, cortical thickness, total BMC, total cross-sectional area, second moment of area along x direction.

References

- Bayraktar, H.H., Morgan, E.F., Niebur, G.L., Morris, G.E., Wong, E.K., Keaveny, T.M., 2004. Comparison of the elastic and yield properties of human femoral trabecular and cortical bone tissue. *J. Biomech.* 37, 27–35.
- Begonia, M., Dallas, M., Johnson, M.L., Thiagarajan, G., 2017. Comparison of strain measurement in the mouse forearm using subject-specific finite element models, strain gaging, and digital image correlation. *Biomech. Model. Mechanobiol.* 16, 1243–1253.
- Birkhold, A.I., Razi, H., Duda, G.N., Weinkamer, R., Checa, S., Willie, B.M., 2014. Mineralizing surface is the main target of mechanical stimulation independent of age: 3d dynamic in vivo morphometry. *Bone* 66, 15–25.
- Bouxsein, M.L., Boyd, S.K., Christiansen, B.A., Guldborg, R.E., Jepsen, K.J., Müller, R., 2010. Guidelines for assessment of bone microstructure in rodents using micro-computed tomography. *J. Bone Miner. Res.* 25, 1468–1486.
- Chen, Y., Dall'Ara, E., Sales, E., Manda, K., Wallace, R., Pankaj, P., Viceconti, M., 2017. Micro-Ct based finite element models of cancellous bone predict accurately displacement once the boundary condition is well replicated: a validation study. *J. Mech. Behav. Biomed. Mater.* 65, 644–651.
- Cheong, V.S., Campos Marin, A., Lacroix, D., Dall'ara, E., 2020. A novel algorithm to predict bone changes in the mouse tibia properties under physiological conditions. *Biomech. Model. Mechanobiol.* 19 (3), 985–1001. Epub 2019 Nov 30.
- Christiansen, B.A., 2016. Effect of micro-computed tomography voxel size and segmentation method on trabecular bone microstructure measures in mice. *BoneKEY Rep.* 5, 136–140.
- Costa, M.C., Tozzi, G., Cristofolini, L., Danesi, V., Viceconti, M., Dall'ara, E., 2017. Micro Finite Element models of the vertebral body: validation of local displacement predictions. *PLoS One* 12, e0180151.
- Crawford, R.P., Cann, C.E., Keaveny, T.M., 2003. Finite element models predict in vitro vertebral body compressive strength better than quantitative computed tomography. *Bone* 33, 744–750.
- Dall'ara, E., Luisier, B., Schmidt, R., Kainberger, F., Zysset, P., Pahr, D., 2013. A nonlinear Qct-based finite element model validation study for the human femur tested in two configurations in vitro. *Bone* 52, 27–38.
- Dall'ara, E., Boudiffa, M., Taylor, C., Schug, D., Fiegle, E., Kennerley, A.J., Damianou, C., Tozer, G.M., Kiessling, F., Müller, R., 2016. Longitudinal imaging of the ageing mouse. *Mech. Ageing Dev.* 160, 93–116.
- Dall'ara, E., Pahr, D., Varga, P., Kainberger, F., Zysset, P., 2012. Qct-based finite element models predict human vertebral strength in vitro significantly better than simulated Dexa. *Osteoporos. Int.* 23, 563–572.
- Gustafson, H.M., Cripton, P.A., Ferguson, S.J., Helgason, B., 2017. Comparison of specimen-specific vertebral body finite element models with experimental digital image correlation measurements. *J. Mech. Behav. Biomed. Mater.* 65, 801–807.
- Holguin, N., Brodt, M.D., Sanchez, M.E., Kotiya, A.A., Silva, M.J., 2013. Adaptation of tibial structure and strength to axial compression depends on loading history in both C57bl/6 and Balb/c mice. *Calcif. Tissue Int.* 93, 211–221.
- Jepsen, K.J., Silva, M.J., Vashishth, D., Guo, X.E., Van Der Meulen, M.C., 2015. Establishing biomechanical mechanisms in mouse models: practical guidelines for systematically evaluating phenotypic changes in the diaphyses of long bones. *J. Bone Miner. Res.* 30, 951–966.
- Kazakia, G.J., Burghardt, A.J., Cheung, S., Majumdar, S., 2008. Assessment of bone tissue mineralization by conventional x-ray microcomputed tomography: comparison with synchrotron radiation microcomputed tomography and ash measurements. *Med. Phys.* 35 (7), 3170–3179.
- Keaveny, T.M., Mcclung, M.R., Genant, H.K., Zanchetta, J.R., Kendler, D., Brown, J.P., Goemaere, S., Recknor, C., Brandi, M.L., Eastell, R., Kopperdahl, D.L., Engelke, K., Fuerst, T., Radcliffe, H.-S., Libanati, C., 2014. Femoral and vertebral strength improvements in postmenopausal women with osteoporosis treated with denosumab. *J. Bone Miner. Res.* 29, 158–165.
- Lu, Y., Boudiffa, M., Dall'ara, E., Bellantuono, I., Viceconti, M., 2016. Development of a protocol to quantify local bone adaptation over space and time: quantification of reproducibility. *J. Biomech.* 2095–2099.
- Lu, Y., Boudiffa, M., Dall'ara, E., Liu, Y., Bellantuono, I., Viceconti, M., 2017. Longitudinal effects of Parathyroid Hormone treatment on morphological, densitometric and mechanical properties of mouse tibia. *J. Mech. Behav. Biomed. Mater.* 75, 244–251.
- Macneil, J.A., Boyd, S.K., 2008. Bone strength at the distal radius can be estimated from high-resolution peripheral quantitative computed tomography and the finite element method. *Bone* 42, 1203–1213.
- Nyman, J.S., Uppuganti, S., Makowski, A.J., Rowland, B.J., Merkel, A.R., Sterling, J.A., Bredbenner, T.L., Perrien, D.S., 2015. Predicting mouse vertebra strength with

- micro-computed tomography-derived finite element analysis. *BoneKey Rep.* 4, 664–664.
- Oliviero, S., Giorgi, M., Dall'ara, E., 2018. Validation of finite element models of the mouse tibia using digital volume correlation. *J. Mech. Behav. Biomed. Mater.* 86, 172–184.
- Oliviero, S., Giorgi, M., Laud, P.J., Dall'ara, E., 2019. Effect of repeated in vivo micro-CT imaging on the properties of the mouse tibia. *PLoS One* 14, e0225127.
- Oliviero, S., Lu, Y., Viceconti, M., Dall'ara, E., 2017. Effect of integration time on the morphometric, densitometric and mechanical properties of the mouse tibia. *J. Biomech.* 65, 203–211.
- Patel, T.K., Brodt, M.D., Silva, M.J., 2014. Experimental and finite element analysis of strains induced by axial tibial compression in young-adult and old female C57Bl/6 mice. *J. Biomech.* 47, 451–457.
- Pepe, V., Oliviero, S., Cristofolini, L., Dall'ara, E., 2020. Regional nanoindentation properties in different locations on the mouse tibia from C57Bl/6 and Balb/C female mice. *Front. Bioeng. Biotechnol.* 8, 478.
- Pereira, A.F., Javaheri, B., Pitsillides, A.A., Shefelbine, S.J., 2015. Predicting cortical bone adaptation to axial loading in the mouse tibia. *J. R. Soc. Interface* 12.
- Pistoia, W., Van Rietbergen, B., Lochmüller, E.M., Lill, C.A., Eckstein, F., Rüeggsegger, P., 2002. Estimation of distal radius failure load with micro-finite element analysis models based on three-dimensional peripheral quantitative computed tomography images. *Bone* 30, 842–848.
- Pottecher, P., Engelke, K., Duchemin, L., Museyko, O., Moser, T., Mitton, D., Vicaut, E., Adams, J., Skalli, W., Laredo, J.D., Bousson, V., 2016. Prediction of hip failure load: in vitro study of 80 femurs using three imaging methods and finite element models—the European fracture study (effect). *Radiology* 280, 837–847.
- Qasim, M., Farinella, G., Zhang, J., Li, X., Yang, L., Eastell, R., Viceconti, M., 2016. Patient-specific finite element estimated femur strength as a predictor of the risk of hip fracture: the effect of methodological determinants. *Osteoporos. Int.* 27, 2815–2822.
- Razi, H., Birkhold, A.I., Zaslansky, P., Weinkamer, R., Duda, G.N., Willie, B.M., Checa, S., 2015. Skeletal maturity leads to a reduction in the strain magnitudes induced within the bone: a murine tibia study. *Acta Biomater.* 13, 301–310.
- Roberts, B.C., Giorgi, M., Oliviero, S., Wang, N., Boudiffa, M., Dall'ara, E., 2019. The longitudinal effects of ovariectomy on the morphometric, densitometric and mechanical properties in the murine tibia: a comparison between two mouse strains. *Bone* 127, 260–270.
- Schileo, E., Dall'ara, E., Taddei, F., Malandrino, A., Schotkamp, T., Baleani, M., Viceconti, M., 2008. An accurate estimation of bone density improves the accuracy of subject-specific finite element models. *J. Biomech.* 41, 2483–2491.
- Schwiedrzik, J., Gross, T., Bina, M., Pretterklieber, M., Zysset, P., Pahr, D., 2016. Experimental validation of a nonlinear μ fe model based on cohesive-frictional plasticity for trabecular bone. *Int. J. Numer. Methods Biomed. Eng.* 32, e02739-n/a.
- Varga, P., Dall'ara, E., Pahr, D.H., Pretterklieber, M., Zysset, P.K., 2011. Validation of an Hr-pqct-based homogenized finite element approach using mechanical testing of ultra-distal radius sections. *Biomech. Model. Mechanobiol.* 10, 431–444.
- Varga, P., Willie, B.M., Stephan, C., Kozloff, K.M., Zysset, P.K., 2020. Finite element analysis of bone strength in osteogenesis imperfecta. *Bone* 133, 115250.
- Viceconti, M., Dall'ara, E., 2019. From bed to bench: how in silico medicine can help ageing research. *Mech. Ageing Dev.* 177, 103–108.
- Wallace, R.J., Pankaj, P., Simpson, A.H.R.W., 2014. Major source of error when calculating bone mechanical properties. *J. Bone Miner. Res.* 29, 2697–2697.
- Wolfram, U., Wilke, H.-J., Zysset, P.K., 2010. Valid μ finite element models of vertebral trabecular bone can be obtained using tissue properties measured with nanoindentation under wet conditions. *J. Biomech.* 43, 1731–1737.
- Yang, H., Albiol, L., Chan, W.-L., Wulsten, D., Seliger, A., Thelen, M., Thiele, T., Spevak, L., Boskey, A., Kornak, U., Checa, S., Willie, B.M., 2017. Examining tissue composition, whole-bone morphology and mechanical behavior of *Corabprx1* mice tibiae: a mouse model of premature aging. *J. Biomech.* 65, 145–153.
- Zhao, S., Arnold, M., Ma, S., Abel, R.L., Cobb, J.P., Hansen, U., Boughton, O., 2018. Standardizing compression testing for measuring the stiffness of human bone. *Bone Jt. Res.* 7, 524–538.
- Zysset, P., Pahr, D., Engelke, K., Genant, H.K., Mcclung, M.R., Kandler, D.L., Recknor, C., Kinzl, M., Schwiedrzik, J., Museyko, O., Wang, A., Libanati, C., 2015. Comparison of proximal femur and vertebral body strength improvements in the Freedom trial using an alternative finite element methodology. *Bone* 81, 122–130.
- Zysset, P.K., Dall'ara, E., Varga, P., Pahr, D.H., 2013. Finite element analysis for prediction of bone strength. *BoneKey Rep.* 2, 386–386.